A CMOS-integrated quantum sensor based on nitrogen-vacancy centres

Donggyu Kim^{1,2,5}, Mohamed I. Ibrahim^{3,4,5}, Christopher Foy^{1,4,5}, Matthew E. Trusheim^{1,4}, Ruonan Han^{3,4,*} and Dirk R. Englund^{1,3,4,*}

The nitrogen-vacancy (NV) centre in diamond can be used as a solid-state quantum sensor with applications in magnetometry, electrometry, thermometry and chemical sensing. However, to deliver practical applications, existing NV-based sensing techniques, which are based on bulky and discrete instruments for spin control and detection, must be replaced by more compact designs. Here we show that NV-based quantum sensing can be integrated with complementary metal-oxide-semiconductor (CMOS) technology to create a compact and scalable platform. Using standard CMOS technology, we integrate the essential components for NV control and measurement—microwave generator, optical filter and photodetector—in a 200 μ m × 200 μ m footprint. With this platform we demonstrate quantum magnetometry with a sensitivity of 32.1 μ T Hz^{-1/2} and simultaneous thermometry.

uantum metrology based on solid-state spins has demonstrated impressive sensing capabilities for various environmental physical quantities. In particular, the NV centre in diamond has emerged as a leading room-temperature quantum sensor for temperature¹⁻⁴, strain⁵⁻⁷, electric fields⁸⁻¹⁰ and magnetic fields¹¹⁻¹⁷, including for atomic species¹⁸⁻²⁵. The capabilities of NV-based quantum metrology are based on its long spin coherence time²⁶ and its efficient optical interface for spin polarization and readout. Furthermore, picotesla magnetic field sensitivity at direct current (d.c.) under ambient conditions has been achieved by interrogating NV centre ensembles²⁷.

Conventional approaches for NV magnetometry, which are based on optically detected magnetic resonance (ODMR)²⁸, involve bulky and discrete off-the-shelf instruments that limit the practical applications and scalability of the approach. NV-ODMR requires a number of specific components: a microwave signal generator, an amplifier and a delivery interface for NV spin manipulation; an optical filter to reject the pump laser; a photodetector for NV spin-dependent fluorescence measurements; a pump laser. In this Article, we report a custom complementary metal–oxide-semiconductor (CMOS) architecture that stacks the microwave inductor, filter and photodiode into a $200\,\mu\text{m}\times200\,\mu\text{m}$ footprint. This extends our previous report²⁹ on a hybrid diamond–CMOS platform by demonstrating ambient quantum vector magnetometry with a twofold improvement in sensitivity, as well as simultaneous thermometry.

Chip-scale quantum sensing

Figure 1a illustrates the device for on-chip ODMR. A diamond slab is irradiated and annealed to produce NV centres at a density of ~0.01 ppm. A 45° cut in the corner of the diamond directs the off-chip green pump beam along the length of the diamond slab. This side excitation reduces the pump laser background into the photodetector located below the diamond. An on-chip microwave generator and inductor drives the NV electron spin transitions.

NV magnetometry detects external magnetic fields via the Zeeman shift induced on the NV's spin ground-state sublevels²⁸, as shown in Fig. 2a. Specifically, an external magnetic field **B** induces an energy shift $\gamma_e B_z$ on the NV ground-state spin triplet ($|m_s=0,\pm 1\rangle$), where B_z is the magnetic field component along the NV symmetry axis. The spin transition frequencies, ν_\pm , between sublevels $|0\rangle$ and $|\pm 1\rangle$, are given by

$$\nu_{\pm} = (D_{\rm gs} - \beta_T \Delta T) \pm \gamma_e B_z \tag{1}$$

where $D_{\rm gs}$ =2.87 GHz is the room-temperature natural ground-state splitting between sublevels $|0\rangle$ and $|\pm 1\rangle$, $\gamma_{\rm e}$ is the electronic gyromagnetic ratio (28 GHz T⁻¹), β_T \approx 74 kHz K⁻¹ (ref. ³⁰) and ΔT is the temperature shift from room temperature. Measuring ν_{\pm} gives B_z and ΔT in their difference and sum, respectively. In addition, measuring B_z for at least three of the four possible NV orientations in diamond (inset, Fig. 1a) quantifies all components of **B** for vector magnetometry^{31–34}.

The NV ground-state transitions ν_\pm are measured by ODMR under green laser excitation, as illustrated in Fig. 2a. The spin magnetic sublevel $|0\rangle$ has a bright cycling transition, where it emits red fluorescence. By contrast, the $|\pm 1\rangle$ can undergo an intersystem crossing into a metastable, dark spin-singlet state, from where it decays back into the $|0\rangle$ sublevel. This has two consequences: optical spin polarization into sublevel $|0\rangle$ and lower average fluorescence of the $|\pm 1\rangle$ spin populations. The microwave field moves spin population between $|0\rangle$ and $|\pm 1\rangle$. Sweeping the applied microwave frequency leads to the ODMR spectra in Fig. 2b, from which ν_\pm are determined.

On-chip microwave generation and delivery

In our chip-scale NV magnetometer, the ground-state spin transitions are driven by the on-chip generated microwave fields. Figure 3a shows the circuitry for on-chip microwave generation and delivery. This circuitry is composed of a phase-locked loop (PLL),

Research Laboratory of Electronics, Massachusetts Institute of Technology, Cambridge, MA, USA. ²Department of Mechanical Engineering, Massachusetts Institute of Technology, Cambridge, MA, USA. ³Microsystems Technology Laboratories, Massachusetts Institute of Technology, Cambridge, MA, USA. ⁴Department of Electrical Engineering and Computer Science, Massachusetts Institute of Technology, Cambridge, MA, USA. ⁵These authors contributed equally: Donggyu Kim, Mohamed I. Ibrahim, Christopher Foy *e-mail: ruonan@mit.edu; englund@mit.edu

NATURE ELECTRONICS ARTICLES

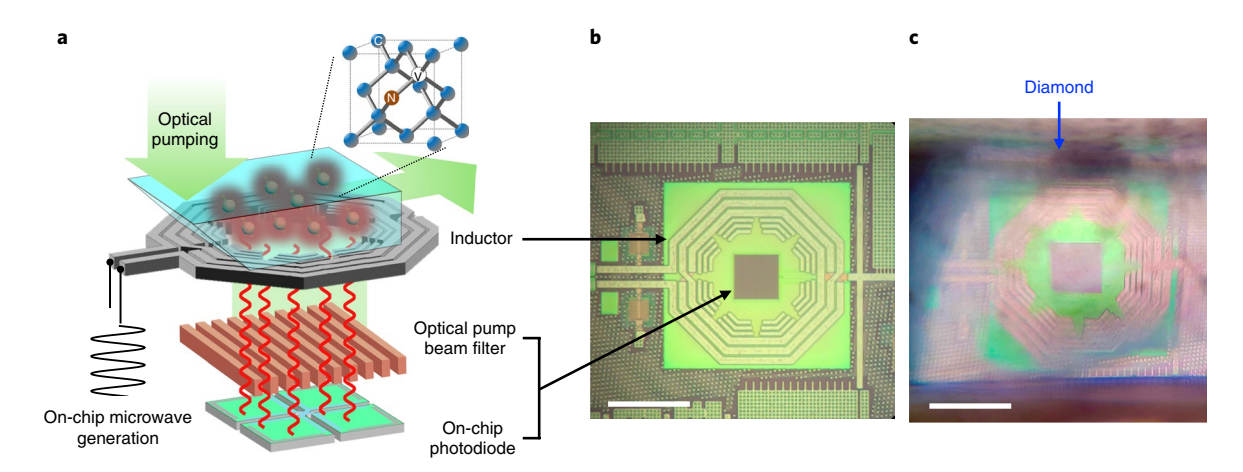


Fig. 1 | CMOS-integrated quantum sensing architecture. a, A green pump laser excites an NV ensemble in the diamond slab. Microwave fields generated on-chip manipulate NV electron spins through an on-chip inductor, leading to ODMR. A metal/dielectric grating absorbs the green pump beam and transmits the NV spin-dependent fluorescence to the on-chip photodiode. Inset: NV atomic structure. **b,c**, Top-view micrographs of the fabricated CMOS chip without (**b**) and with (**c**) the diamond slab. Scale bars, 200 μm.

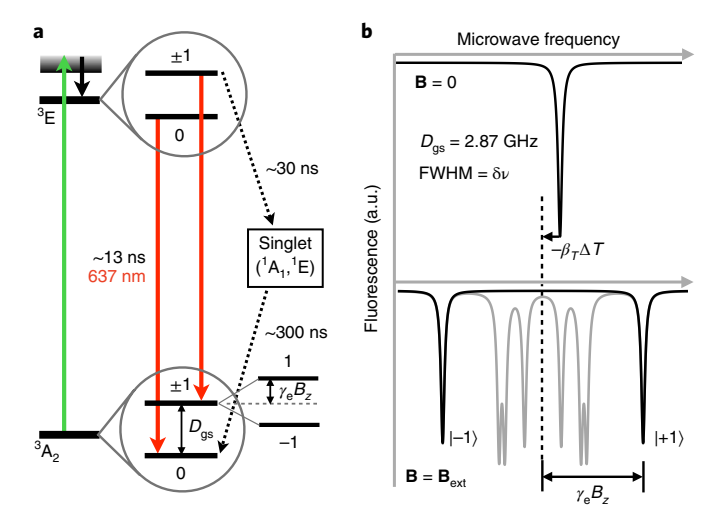


Fig. 2 | NV energy level diagram and ODMR spectra. **a**, NV energy level diagram: the green optical pump (green arrow) excites NV electrons from 3A_2 to 3E . NV centres then emit red fluorescence by radiative decay (red arrow). The intersystem crossing rate (black dashed arrow) depends on the NV spin states, resulting in spin-dependent fluorescence. **b**, Top: for **B** = 0, the ODMR spectrum shows one fluorescence dip for $\nu_\pm = D_{\rm gs}$. Bottom: for an external magnetic field ${\bf B}_{\rm extr}$ this resonance splits into two Zeeman-shifted spin transitions (black curve), whose difference (mean) gives B_z (ΔT). The grey curves show ODMR for the other three possible NV orientations.

a current driver and a resonant loop inductor. The PLL generates the microwave sweep signal from 2.6 GHz to 3.1 GHz, required for the ODMR experiment. The main component of this loop is an onchip voltage-controlled ring oscillator (VCO) with three differential inverter stages. The use of a ring VCO 35 avoids any large-size inductor and minimizes the crosstalk between the oscillator and the microwave inductor, which drives the NV ensemble. The mutual-locking inverter pair (for example, INV $_2$ in Fig. 3a) forms a latch and ensures the differential phases between the left and right branches of the VCO. The frequency tunability of the oscillator is realized via three pairs of MOS variable capacitors (for example, $\rm C_{VCO}$ in Fig. 3a), where the capacitance changes from 22 fF to 75 fF when

the PLL control voltage $V_{\rm curl}$ varies from 0 to 5 V. The entire PLL is closed with off-chip components to enhance the stability and decrease the phase noise of the signal. Further details are provided in the Methods.

The microwave fields are delivered to the NV ensemble through the loop inductor (Fig. 3a) implemented on the topmost copper layer (Metal 9, see Methods for details) with a thickness of 3.4 µm. To efficiently deliver the microwave field, the loop inductor and a pair of shunt capacitors (C₁ and C₂ in Fig. 3a) form a resonating load for the current driver. C1 and C2 are MOS variable capacitors with capacitance ranging from 312 fF to 1.4 pF. By electrically tuning them via $V_{\rm tune}$, the load resonates near $D_{\rm gs}$. This current driver fed by the output of the ring VCO produces oscillating current in the inductor at the VCO microwave frequency. To improve the performance of this inductor for advanced NV sensing protocols³⁶, we need to increase the applied microwave field amplitude. The amplitude is enhanced by a factor Q of the driver d.c. bias current ($I_{\text{bias}} \approx 5 \,\text{mA}$ from a 2.5 V power supply), where $Q(\sim 15)$ is the quality factor of the inductor. In addition, we use a three-turn loop to multiply the microwave field strength. Overall, we have 25× enhanced microwave field strength compared to a non-resonant single-turn loop (as plotted in Fig. 3b). With an outer diameter of 236 µm, the loop exhibits an inductance of ~3 nH. In addition, the aforementioned sensing protocols also require highly uniform microwave fields over the excitation volume. To achieve this, three capacitive parasitic loops are inserted²⁹. We tailor the radius of these loops so that their opposite induced field homogenizes the overall generated field. Another degree of freedom is provided by the capacitive gaps in the parasitic loops. This controls the amount of current flowing in these loops. We thus optimized these two parameters (the parasitic loop radius and the capacitive gap) for the three parasitic loops to achieve >95% uniformity. Detailed dimensions of the microwave launcher and loop inductor are provided in the Methods and Supplementary Fig. 1, respectively. The spectral purity (phase noise) of the microwave is -90 dBc Hz⁻¹ at an offset frequency (also the FM modulation frequency $f_{\rm m}$) of 1.5 kHz.

On-chip spin readout

The NV spin transitions are detected using an on-chip photodetector. The green laser pump beam is filtered by a CMOS-compatible periodic metal-dielectric structure (Fig. 4a) in the Metal 8 interconnect layer. Specifically, incident light couples to the surface plasmon polariton at the metal-dielectric interface, where the green pump

ARTICLES NATURE ELECTRONICS

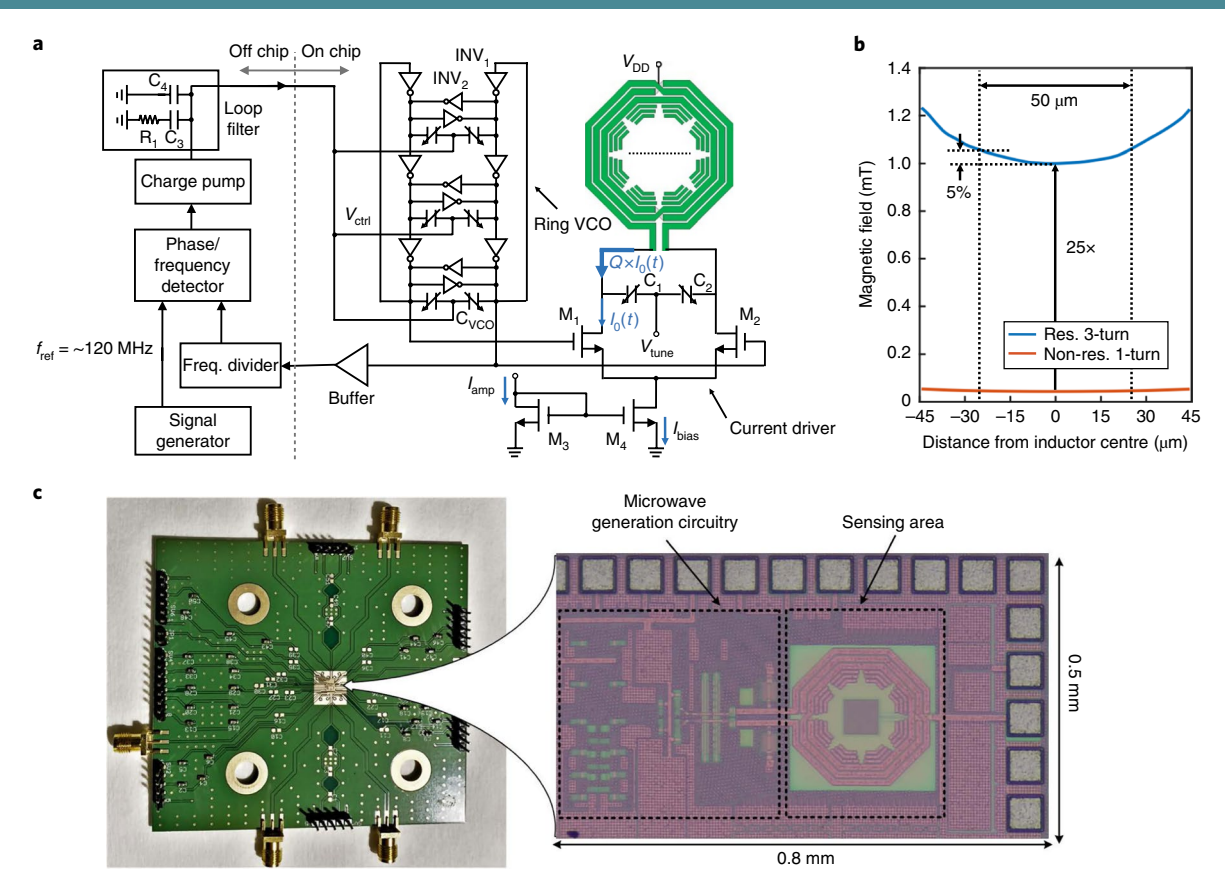


Fig. 3 | On-chip CMOS microwave generation and inductor characteristics. **a**, Schematic of the microwave generation circuitry. **b**, High-frequency electromagnetic fields simulations for the on-chip inductor. The magnetic field amplitude is plotted as a function of distance from the inductor centre (dashed line in **a**). The resonant multi-turn loop inductor (blue) produces 25× higher amplitude compared to the non-resonant single turn inductor (red) at the same d.c. current. Insertion of the parasitic capacitive loops yields a microwave uniformity of 95% over 50 μm. **c**, Optical micrograph of the CMOS chip (right) and photograph of the printed circuit board for testing (left).

light rapidly decays due to frequency-dependent ohmic loss^{37,38}. The inset in Fig. 4a presents the intensity map for the green (λ = 532 nm, top) and red (λ = 700 nm, bottom) light, showing ~95% and ~5% absorption with the metal–dielectric structure, respectively.

The photodiode consists of a p+/n-well/p-substrate junctions (inset, Fig. 4b), which is preferable for long wavelength detection³⁹. Because we place the photodiode with its conductive layers below the inductor (Fig. 1a), large eddy currents near 2.87 GHz can be induced. This reduces the quality factor of the inductor, resulting in microwave amplitude reduction. We can reduce this eddy current by half by dividing the photodiode area into four sub-areas as shown in Fig. 4b (see Methods for a detailed analysis). Furthermore, the anode/cathode connectors are arranged in a similar way to the patterned ground shielding used in CMOS inductors⁴⁰. This arrangement avoids any closed loops, which helps to cut the eddy current that may flow in the metallic connections. The photodiode has a measured responsivity of 0.23 A W⁻¹ at a wavelength of 532 nm, which corresponds to a quantum efficiency of 0.54.

On-chip ODMR detection and quantum sensing

We detect NV-ODMR with a lock-in technique. The green laser beam continuously excites the NV ensemble, and the frequency-modulated (FM) microwave fields ($f_{\rm m}=1.5\,{\rm kHz}$, modulation depth of 6 MHz) drive the NV electron spin transition. The spin-dependent fluorescence produces photocurrent within the on-chip photodiode (Fig. 4b). We read out the modulated photocurrent with the voltage drop across a 50 Ω resistor at $f_{\rm m}$ with 1 s integration time, which corresponds to an equivalent noise bandwidth of 0.078 Hz

(considering the filter roll-off of 24 dB oct⁻¹) with a Stanford Research Systems lock-in amplifier (SR865A). The use of the lock-in amplifier rejects the d.c. current offset of the photodiode, which is caused by the unmodulated green laser, and avoids the low-frequency flicker noise accordingly.

Figure 5a shows the lock-in signal for the ODMR experiment under zero external magnetic field applied. This spectrum corresponds to the derivative of the ODMR spectrum shown in Fig. 2b. Next, we align a permanent magnet (6.27 mT) to split the spin transitions of the four NV orientations. Figure 5b plots the ODMR spectrum, which exhibits the expected eight spin transitions (Fig. 2b). The use of the corresponding four NV ensembles enables vector magnetometry. In particular, we note the spin transitions at ν_- = 2.8303 GHz and ν_+ = 2.9330 GHz of the NV ensemble.

Monitoring the lock-in signal V at ν_- and ν_+ enables independent measurements of the magnetic field and temperature, as described above. Specifically, the sum of the lock-in signal change ΔV at ν_\pm is proportional to ΔT , while the difference provides ΔB_z :

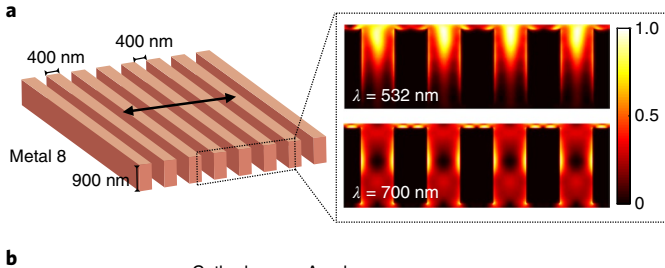
$$\Delta T = \frac{1}{2\beta_T} \left(\frac{\Delta V}{\mathrm{d}V/\mathrm{d}f} \Big|_{\nu_+} + \frac{\Delta V}{\mathrm{d}V/\mathrm{d}f} \Big|_{\nu_-} \right) \tag{2}$$

and

$$\Delta B_z = \frac{1}{2\gamma_e} \left(\frac{\Delta V}{\mathrm{d}V/\mathrm{d}f} \bigg|_{\nu_+} - \frac{\Delta V}{\mathrm{d}V/\mathrm{d}f} \bigg|_{\nu_-} \right) \tag{3}$$

NATURE ELECTRONICS

Figure 5c plots the detected ΔB_z induced by an electromagnet (blue) and the measured centre frequency shift (red). The plotted centre frequency could be converted to a temperature after β_T calibration.



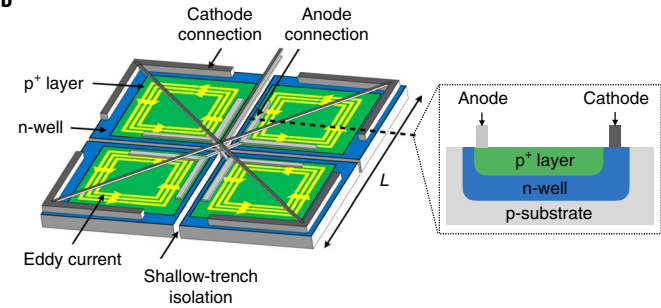


Fig. 4 | On-chip detection of NV spin-dependent fluorescence. a, CMOScompatible optical pump beam filter: the periodic metal-dielectric grating absorbs the green laser light. Inset: finite-difference time-domain (FDTD) calculation of the optical intensity map inside the structure for green (top) and red (bottom) light. The incident light polarization is perpendicular to the grating line. b, Photodiode geometry: the photodiode area is divided into four sub-areas, isolated by shallow trenches to reduce the eddy current (yellow loops) losses. Inset: cross-section along the dashed line in the main panel.

The magnetic field sensitivity is given by the following relation:

$$S = \frac{\sigma_{B_z}}{\sqrt{\text{ENBW}}} \tag{4}$$

where σ_{B_z} is the noise in ΔB_z measurements and ENBW is the equivalent noise bandwidth of the lock-in detector. In our measurement, ENBW = $5/(64\tau)$ with a time constant τ of 1 s, accounting for the 24 dB oct⁻¹ of the lock-in amplifier filter roll-off. By measuring σ_{B_n} of 6.3 µT from the modulated spin-dependent fluorescence (inset, Fig. 5c), we determine a d.c. magnetic field sensitivity of 32.1 μ T Hz^{-1/2}, which includes an additional $\sqrt{2}$ factor of the ν_+ and ν_- signal average. This d.c. magnetic field sensitivity is limited by the noise detected in the ENBW at $f_{\rm m} = 1.5 \,\rm kHz$. Figure 5d plots the noise spectral density measured at ν_{-} (no temperature compensation) using the lock-in amplifier, where the noise floor is $\sim 35 \,\mathrm{nV}\,\mathrm{Hz}^{-1/2}$. This noise is then converted to the magnetic field sensitivity with the slope at ν_{-} and γ_{e} (plotted in the right y axis in Fig. 5d).

The achieved magnetic field sensitivity is orders of magnitude worse than the best d.c. sensitivities reported: 290 and 28 pT Hz^{-1/2} for vector²⁷ and scalar⁴¹ magnetometry, respectively, to the best of our knowledge. Our sensitivity is mainly limited by the green laser intensity noise (see Methods for detailed noise estimation). However, this performance can be improved by (1) including metal gratings in multiple CMOS metal layers based on the wavelengthdependent Talbot effect⁴² and (2) fabricating a resonant grating⁴³ in diamond. These also attenuate the green laser and consequently reduce the laser intensity noise by several orders of magnitude. In addition, using a diamond waveguide geometry²⁷—possibly with a higher NV density44 (~10 ppm)—should increase the signal-tonoise ratio by orders of magnitudes. Moreover, dynamical decoupling sequences^{28,36} can improve the sensitivity by a few orders of magnitude for measuring magnetic fields at frequencies above the NV decoherence rate.

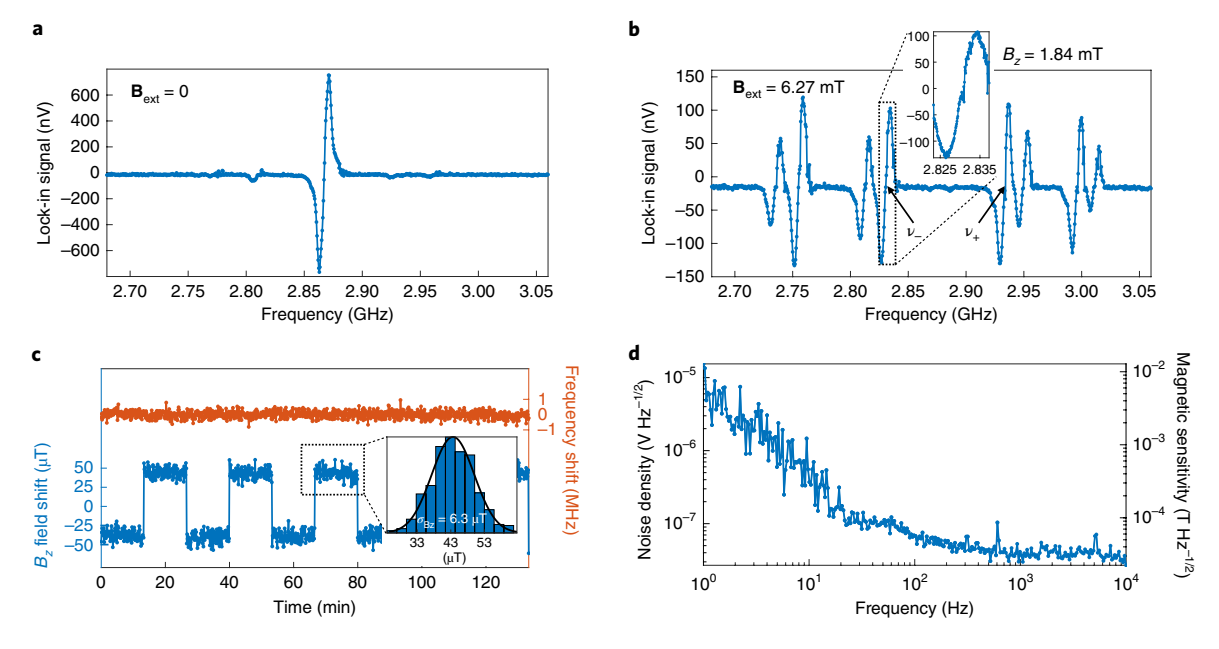


Fig. 5 | On-chip detection of ODMR and NV-based quantum magnetometry. a, FM lock-in signal of NV spin-dependent fluorescence at zero external magnetic field (in addition to $B \sim 100 \,\mu\text{T}$ of Earth's magnetic field). **b**, FM lock-in signal with a permanent magnet ($B = 6.27 \,\text{mT}$): B_z is the magnetic field along the NV axis with the spin transition at ν_{\pm} . The linewidth of the ODMR is 7 MHz. Slopes dV/df at ν_{-} = 2.8303 GHz and ν_{+} = 2.9330 GHz are 42.969 nV MHz⁻¹ and 42.450 nV MHz⁻¹, respectively. \mathbf{c} , On-chip magnetometry (blue) and temperature effect (red) separation: lock-in signals at ν_{+} are observed while switching the polarity of the external electromagnet with a period of 26 min. Inset: histogram of measured magnetic field B, with a s.d. of 6.3 μ T. This uncertainty corresponds to a magnetic field sensitivity of 32.1 μ T Hz^{-1/2}. After calibration of β_T , the plotted centre frequency (red) could be converted to a temperature. Measurement is conducted with a time constant of 1s, **d**. Noise spectral density monitored at ν .

ARTICLES NATURE ELECTRONICS

One component not presently integrated into our diamond-CMOS platform is the pump laser for NV optical excitation. This optical pump can be integrated into our platform by using a chip-scale laser diode⁴⁵, green vertical-cavity surface-emitting lasers⁴⁶ or CMOS-compatible waveguided delivery of the optical pump beam⁴⁷. We note that CMOS integration of all currently off-chip electronic components, such as the PLL with frequency modulation and the lock-in amplifier, has been demonstrated in previous research⁴⁸. This suggests the feasibility of a millimetre-scale form factor for future quantum-sensing systems.

Conclusions

We have reported chip-scale quantum magnetometry by integrating diamonds with CMOS technology, creating an architecture in which the essential components to detect NV-ODMR-a microwave generator, an inductor, an optical pump beam filter and a photodetector—are fabricated throughout the CMOS multilayers. NV spin ensembles integrated on the CMOS chip measure external magnetic fields with a sensitivity of 32.1 $\mu T\,Hz^{-1/2},$ and this compact spin-CMOS platform can be extended to on-chip sensing of other quantities such as electric fields. We emphasize that our CMOS circuit provides direct physical interactions with the NV quantum states beyond electronic input/output signalling⁴⁹. In addition to chip-scale quantum sensing capability, our CMOS-based spin control and readout scheme can uniquely provide a scalable solution for implementing spin quantum-bit controls. This is, in particular, essential to developing a large-scale quantum system⁴⁹⁻⁵², which would enable quantum-enhanced sensing^{36,53,54} and quantum information processing⁵⁵⁻⁵⁷.

Methods

Diamond preparation and CMOS chip design. To avoid the direct injection of the green laser pump beam onto the CMOS, we cut the CVD-grown diamond single crystal (Element 6) as shown in Fig. 1a, enabling optical pumping in parallel with the CMOS-diamond interface with total internal reflection. The diamond was irradiated by an electron beam with a dosage of $1 \times 10^{18} \, e^- \, cm^{-2}$ at $1 \, MeV$, then annealed for 2h at 850°C. The diamond slab was picked and placed on the CMOS chip under a microscope, and immersion oil was used in the diamond-CMOS interface to adhere the two together. This also minimized the fluorescence loss by reducing the refractive index difference. The chips were fabricated with standard 65 nm low power CMOS technology (TSMC), producing 1.2 V and 2.5 V MOSFET transistors; the latter, with a minimum gate length of 280 nm, were used in this work. The CMOS technology also produced nine copper interconnect layers (Metal 1-Metal 9), an aluminium pad/redistribution layer and a top nitride layer for surface passivation. which we removed by reactive ion etching to reduce the associated red fluorescence. No additional post-processing other than etching of the passivation layer was carried out. The total chip area, including the electronic/photonic components and the bond pads, was $0.8 \times 0.5 \, \text{mm}^2$. In Fig. 3, the sizes (gate width/gate length) of transistors M_1 - M_4 are $80 \,\mu\text{m}/280 \,\text{nm}$, $80 \,\mu\text{m}/280 \,\text{nm}$, $72 \,\mu\text{m}/500 \,\text{nm}$ and $720 \,\mu\text{m}/500 \,\text{nm}$, respectively. Inside each inverter stage (for example, INV₁ in Fig. 3a) of the on-chip ring VCO, the sizes of the NMOS and PMOS are $24 \mu m/280 nm$ and $54 \mu m/280 nm$, respectively. Inside each latch inverter (for example, INV, in Fig. 3a), the NMOS and PMOS sizes are $5.2 \,\mu\text{m}/280 \,\text{nm}$ and $12 \,\mu\text{m}/280 \,\text{nm}$, respectively.

Measurement set-up. The measurement set-up is arranged as follows. A linearly polarized DPSS green laser beam (500 mW, $\lambda = 532$ nm, Verdi G2, Coherent) is delivered to the diamond through a telescope with $f_1 = 35$ mm and $f_2 = 150$ mm. The beam diameter incident on the diamond is ~500 µm. A half-wave plate is used to rotate the polarization of the laser beam to maximize the laser absorption through the periodic metal/dielectric structure in the Metal 8 layer. The CMOS chip is wire-bonded on a printed circuit board. Its internal ring VCO, combined with an off-chip synthesizer circuit (AD9525, Analog Devices) including a charge pump, a phase/frequency detector and a frequency divider, form a phase-locked loop (PLL). The VCO output signal is frequency-divided by 24 and then compared to a 120 MHz reference signal provided by an external signal source (HP ESG- $\mathrm{D4000A}).$ The loop filter of the PLL is a typical second-order low-pass filter and the values of the components shown in Fig. 3a are $R_1 = 0.4 \text{ k}\Omega$, $C_3 = 4.5 \text{ nF}$ and $C_4 = 150 \,\mathrm{pF}$. A permanent magnet is used in Fig. 5b to split the NV orientations. The square-wave magnetic field applied in Fig. 5c is generated by an electromagnet. An alternating electric current is used to avoid magnetization. A lens system is used because our laser is located far from the sample for experimental convenience, although we note that the lens system could be avoided if the laser were to be positioned near the CMOS chip.

Eddy current analysis. For a square photodiode with a side length L, the eddy current power $P_{\rm eddy}$ is quadratically proportional to the change in magnetic flux $\mathrm{d}\phi(t)/\mathrm{d}t$:

$$P_{
m eddy} \propto rac{\left({
m d}\phi(t)/{
m d}t
ight)^2}{R} \propto rac{L^4 \left(rac{{
m d}B}{{
m d}t}
ight)^2}{L} \propto L^3 \left(rac{{
m d}B}{{
m d}t}
ight)^2$$

where *t* is the time, *R* is the resistance and *B* is the magnetic field generated by the loop inductor in Metal 9. By dividing the photodiode active area into $N \times N$ sub-areas, the eddy current is reduced by $N^2 \times (L/N)^3/L^3 = 1/N$.

Noise estimation. In our experiment, the measurement noise (38 nV Hz^{-1/2} at $f_{\rm m}=1.5$ kHz) primarily derives from the green laser intensity noise due to the limited performance of the optical filters. This laser intensity noise is orders of magnitude larger than other noise sources: (1) the NV red fluorescence shot noise is $R\sqrt{2q^2 h_D}\sim 9$ pV Hz^{-1/2} at $f_{\rm m}=1.5$ kHz, where $i_{\rm D}\sim (1/C)(100$ nV)/R, ODMR contrast $C\sim0.02$, $q=1.6\times10^{-19}$ C and R=50 Ω ; (2) the thermal noise of 50 Ω resistance is ~ 0.9 nV Hz^{-1/2}, which is used to convert the photocurrent to voltage; (3) the noise converted from the microwave spectral purity ($\phi_p=-90$ dBc Hz⁻¹ at $f_{\rm m}$) is $\propto V_s\phi_pf_{\rm m}\beta\sim 1$ fV Hz^{-1/2}. Here, V_s is the signal voltage amplitude and β is the slope of the FM-ODMR curve. We assume that $\phi_p\ll 1$.

Data availability

The data that support the plots within this paper and other findings of this study are available from the corresponding author upon reasonable request.

Received: 1 October 2018; Accepted: 20 June 2019; Published online: 23 July 2019

References

- Kucsko, G. et al. Nanometre-scale thermometry in a living cell. Nature 500, 54–58 (2013)
- Neumann, P. et al. High-precision nanoscale temperature sensing using single defects in diamond. Nano Lett. 13, 2738–2742 (2013).
- Plakhotnik, T., Doherty, M. W., Cole, J. H., Chapman, R. & Manson, N. B. All-optical thermometry and thermal properties of the optically detected spin resonances of the NV⁻ center in nanodiamond. *Nano Lett.* 14, 4989–4996 (2014).
- Laraoui, A. et al. Imaging thermal conductivity with nanoscale resolution using a scanning spin probe. Nat. Commun. 6, 8954 (2015).
- Ovartchaiyapong, P., Lee, K. W., Myers, B. A. & Jayich, A. C. B. Dynamic strain-mediated coupling of a single diamond spin to a mechanical resonator. *Nat. Commun.* 5, 4429 (2014).
- Teissier, J., Barfuss, A., Appel, P., Neu, E. & Maletinsky, P. Strain coupling of a nitrogen-vacancy center spin to a diamond mechanical oscillator. *Phys. Rev. Lett.* 113, 020503 (2014).
- Trusheim, M. E. & Englund, D. Wide-field strain imaging with preferentially aligned nitrogen-vacancy centers in polycrystalline diamond. *New J. Phys.* 18, 123023 (2016).
- 8. Dolde, F. et al. Electric-field sensing using single diamond spins. *Nat. Phys.* **7**, 459–463 (2011).
- Chen, E. H. et al. High-sensitivity spin-based electrometry with an ensemble of nitrogen-vacancy centers in diamond. Phys. Rev. A 95, 053417 (2017).
- Broadway, D. A. et al. Spatial mapping of band bending in semiconductor devices using in situ quantum sensors. Nat. Electron. 1, 502–507 (2018).
- Maze, J. et al. Nanoscale magnetic sensing with an individual electronic spin in diamond. Nature 455, 644–647 (2008).
- Balasubramanian, G. et al. Nanoscale imaging magnetometry with diamond spins under ambient conditions. *Nature* 455, 648–651 (2008).
- Grinolds, M. et al. Subnanometre resolution in three-dimensional magnetic resonance imaging of individual dark spins. *Nat. Nanotechnol.* 9, 279–284 (2014).
- Jensen, K. et al. Cavity-enhanced room-temperature magnetometry using absorption by nitrogen-vacancy centers in diamond. *Phys. Rev. Lett.* 112, 160802 (2014).
- 15. Wolf, T. et al. Subpicotesla diamond magnetometry. *Phys. Rev. X* 5, 041001 (2015).
- Glenn, D. R. et al. Single-cell magnetic imaging using a quantum diamond microscope. Nat. Methods 12, 736–738 (2015).
- Boss, J. M., Cujia, K., Zopes, J. & Degen, C. L. Quantum sensing with arbitrary frequency resolution. Science 356, 837–840 (2017).
- Mamin, H. et al. Nanoscale nuclear magnetic resonance with a nitrogenvacancy spin sensor. Science 339, 557–560 (2013).
- Staudacher, T. et al. Nuclear magnetic resonance spectroscopy on a (5-nanometer)³ sample volume. Science 339, 561–563 (2013).
- Häberle, T., Schmid-Lorch, D., Reinhard, F. & Wrachtrup, J. Nanoscale nuclear magnetic imaging with chemical contrast. *Nat. Nanotechnol.* 10, 125–128 (2015).

NATURE ELECTRONICS ARTICLES

- Rugar, D. et al. Proton magnetic resonance imaging using a nitrogen-vacancy spin sensor. Nat. Nanotechnol. 10, 120-124 (2015).
- Aslam, N. et al. Nanoscale nuclear magnetic resonance with chemical resolution. Science 357, 67–71 (2017).
- Lovchinsky, I. et al. Nuclear magnetic resonance detection and spectroscopy of single proteins using quantum logic. Science 351, 836–841 (2016).
- 24. Lovchinsky, I. et al. Magnetic resonance spectroscopy of an atomically thin material using a single-spin qubit. *Science* **355**, 503–507 (2017).
- Glenn, D. R. et al. High-resolution magnetic resonance spectroscopy using a solid-state spin sensor. *Nature* 555, 351–354 (2018).
- Balasubramanian, G. et al. Ultralong spin coherence time in isotopically engineered diamond. Nat. Mater. 8, 383–387 (2009).
- 27. Clevenson, H. et al. Broadband magnetometry and temperature sensing with a light-trapping diamond waveguide. *Nat. Phys.* 11, 393–397 (2015).
- Taylor, J. et al. High-sensitivity diamond magnetometer with nanoscale resolution. Nat. Phys. 4, 810–816 (2008).
- Ibrahim, M. I., Foy, C., Kim, D., Englund, D. R. & Han, R. Roomtemperature quantum sensing in CMOS: on-chip detection of electronic spin states in diamond color centers for magnetometry. In *Proceedings of IEEE* VLSI Circuits Symposium 249–250 (IEEE, 2018).
- Acosta, V. et al. Temperature dependence of the nitrogen-vacancy magnetic resonance in diamond. *Phys. Rev. Lett.* 104, 070801 (2010).
- Maertz, B., Wijnheijmer, A., Fuchs, G., Nowakowski, M. & Awschalom, D. Vector magnetic field microscopy using nitrogen vacancy centers in diamond. *Appl. Phys. Lett.* 96, 092504 (2010).
- Wang, P. et al. High-resolution vector microwave magnetometry based on solid-state spins in diamond. *Nat. Commun.* 6, 6631 (2015).
- Clevenson, H. et al. Robust high-dynamic-range vector magnetometry with nitrogen-vacancy centers in diamond. Appl. Phys. Lett. 112, 252406 (2018).
- Schloss, J. M., Barry, J. F., Turner, M. J. & Walsworth, R. L. Simultaneous broadband vector magnetometry using solid-state spins. *Phys. Rev. Appl.* 10, 034044 (2018).
- 35. Razavi, B. RF Microelectronics (Prentice Hall, 1998).
- Degen, C. L., Reinhard, F. & Cappellaro, P. Quantum sensing. Rev. Mod. Phys. 89, 035002 (2017).
- Zayats, A. V., Smolyaninov, I. I. & Maradudin, A. A. Nano-optics of surface plasmon polaritons. *Phys. Rep.* 408, 131–314 (2005).
- Hong, L., Li, H., Yang, H. & Sengupta, K. Fully integrated fluorescence biosensors on-chip employing multi-functional nanoplasmonic optical structures in CMOS. *IEEE J. Solid-State Circuits* 52, 2388–2406 (2017).
- Murari, K., Etienne-Cummings, R., Thakor, N. & Cauwenberghs, G. Which photodiode to use: a comparison of CMOS-compatible structures. *IEEE Sens. J.* 9, 752–760 (2009).
- Yue, C. P. & Wong, S. S. On-chip spiral inductors with patterned ground shields for Si-based RF ICs. IEEE J. Solid-State Circuits 33, 743–752 (1998).
- 41. Chatzidrosos, G. et al. Miniature cavity-enhanced diamond magnetometer. *Phys. Rev. Appl.* **8**, 044019 (2017).
- 42. Wen, J., Zhang, Y. & Xiao, M. The Talbot effect: recent advances in classical optics, nonlinear optics, and quantum optics. *Adv. Opt. Photon.* 5, 83–130 (2013).
- 43. Peng, S. & Morris, G. M. Resonant scattering from two-dimensional gratings. *J. Opt. Soc. Am. A* 13, 993–1005 (1996).
 44. Acosta, V. et al. Diamonds with a high density of nitrogen-vacancy centers
- Acosta, V. et al. Diamonds with a high density of nitrogen-vacancy centers for magnetometry applications. *Phys. Rev. B* 80, 115202 (2009).
- Oeckinghaus, T. et al. A compact, diode laser based excitation system for microscopy of NV centers. Rev. Sci. Instrum. 85, 073101 (2014).
- Kasahara, D. et al. Demonstration of blue and green GaN-based verticalcavity surface-emitting lasers by current injection at room temperature. *Appl. Phys. Express* 4, 072103 (2011).
- Moss, D. J., Morandotti, R., Gaeta, A. L. & Lipson, M. New CMOScompatible platforms based on silicon nitride and hydex for nonlinear optics. *Nat. Photon.* 7, 597–607 (2013).

- 48. Wang, C. et al. An on-chip fully-electronic molecular clock based on sub-THz rotational spectroscopy. *Nat. Electron.* 1, 421–427 (2018).
- Charbon, E. et al. 15.5 cryo-CMOS circuits and systems for scalable quantum computing. In *Proceedings of IEEE International Solid-State Circuits* Conference (ISSCC) 264–265 (IEEE, 2017).
- 50. Yao, N. Y. et al. Scalable architecture for a room temperature solid-state quantum information processor. *Nat. Commun.* **3**, 800 (2012).
- Veldhorst, M., Eenink, H., Yang, C. & Dzurak, A. Silicon CMOS architecture for a spin-based quantum computer. *Nat. Commun.* 8, 1766 (2017).
- Patra, B. et al. Cryo-CMOS circuits and systems for quantum computing applications. *IEEE J. Solid-State Circuits* 53, 309–321 (2018).
- Giovannetti, V., Lloyd, S. & Maccone, L. Advances in quantum metrology. Nat. Photon. 5, 222–229 (2011).
- Unden, T. et al. Quantum metrology enhanced by repetitive quantum error correction. *Phys. Rev. Lett.* 116, 230502 (2016).
- Bernien, H. et al. Heralded entanglement between solid-state qubits separated by three metres. *Nature* 497, 86–90 (2013).
- 56. Pfaff, W. et al. Unconditional quantum teleportation between distant solid-state quantum bits. *Science* **345**, 532–535 (2014).
- Humphreys, P. C. et al. Deterministic delivery of remote entanglement on a quantum network. *Nature* 558, 268–273 (2018).

Acknowledgements

This research is supported in part by the Army Research Office Multidisciplinary University Research Initiative (ARO MURI) biological transduction programme. D.K. acknowledges financial support from the Kwanjeong Educational Foundation. M.I.I. acknowledges support from the Singaporean-MIT Research Alliance (SMART) and the MIT Center of Integrated Circuits and Systems. C.F. acknowledges support from Master Dynamic Limited and from the National Science Foundation (NSF) Research Advanced by Interdisciplinary Science and Engineering (RAISE) Transformational Advances in Quantum Systems (TAQS). M.E.T. acknowledges support by an appointment to the Intelligence Community Postdoctoral Research Fellowship Program at MIT, administered by Oak Ridge Institute for Science and Education through an interagency agreement between the US Department of Energy and the Office of the Director of National Intelligence.

Author contributions

D.R.E. and R.H. initially conceived the diamond–CMOS integration. M.I.I. conceived the idea of stacking the microwave inductor, plasmonic filter and photodiode in a 3D architecture. M.I.I., C.F. and D.K. contributed to chip specifications, design and the experiment. M.I.I. constructed the CMOS chip prototype. D.K. performed FDTD simulations for the optical filter design and the diamond transfer on the CMOS chip. C.F. prepared the control software for the experiment. C.F. and D.K. constructed the optical set-up and etched the CMOS passivation layers. All authors contributed to discussion of the experimental results and writing of the manuscript.

Competing interests

The chip-scale spin control and detection scheme in this work has been filed in a United States provisional patent application (62/623151).

Additional information

Supplementary information is available for this paper at https://doi.org/10.1038/s41928-019-0275-5.

Reprints and permissions information is available at www.nature.com/reprints.

Correspondence and requests for materials should be addressed to R.H. or D.R.E.

Publisher's note: Springer Nature remains neutral with regard to jurisdictional claims in published maps and institutional affiliations.

© The Author(s), under exclusive licence to Springer Nature Limited 2019